Journal of Alloys and Compounds 509 (2011) 4688–4695

Contents lists available at ScienceDirect

Journal of Alloys and Compounds

journal homepage: www.elsevier.com/locate/jallcom

Thickness dependence of crystalline state in FeZrNbCuB thin films obtained by sputter deposition

Marco Coïsson[a,*], Federica Celegato[a], Elena S. Olivetti[a], Paola Tiberto[a], Franco Vinai[a], Shashank N. Kane[b], Elena A. Gan'shina[c], Andrey I. Novikov[c], Nikolai S. Perov[c]

[a] INRIM, Electromagnetism Division, strada delle Cacce 91, I-10135 Torino, Italy
[b] School of Physics, D.A. University, Khandwa Road, Indore 452017, India
[c] Moscow State University, 119991 Moscow, Russia

ARTICLE INFO

Article history:
Received 30 November 2010
Received in revised form 3 January 2011
Accepted 4 January 2011
Available online 13 January 2011

Keywords:
Amorphous and nanocrystalline magnetic materials
Thin films
Thermal treatments

ABSTRACT

Differential scanning calorimetry, hysteresis measurements, X-ray diffraction, Mössbauer spectroscopy and transversal Kerr effect have been used to study the thickness and temperature dependence of magnetic properties and crystalline state of $Fe_{84}Zr_{3.5}Nb_{3.5}B_8Cu_1$ (at.%) thin films. Results indicate that a decrease of the saturation magnetization with increasing film thickness can be ascribed to the presence of a crystalline α-Fe phase at the early stages of film growth, followed by the deposition of the amorphous alloy. Thinner films, which have a significant crystalline phase in the as-prepared state, display less prominent crystallization features, whereas thicker films, with a significant amorphous phase in the as-prepared state, are characterized by much more pronounced crystallization effects, that are confirmed by Mössbauer and Transversal Kerr Effect measurements. Progressive thinning of a film by means of sputter etching allows to reduce the amorphous component, leading to the expected increase of saturation magnetization as the thickness decreases.

1. Introduction

Amorphous and nanocrystalline magnetic materials have been widely studied in form of bulk ingots, ribbons and microwires because of their soft magnetic properties [1–3], their resistance to oxidation and corrosion [4], the possibility to tune their coercive field and magnetic anisotropy by means of low-temperature thermal treatments [5,6], with or without the application of a mechanical stress or a magnetic field. Today, amorphous and nanocrystalline magnetic materials are used as sensing elements in sensors of magnetic fields, stresses, vibrations or position [7,8], and as power cores for transformers and in other power applications [9,10].

More recently, these families of magnetic materials have gained the attention of the community of researchers working on thin films; in fact, their soft magnetic properties and high permeability make them interesting for a number of applications, including soft underlayers for perpendicular recording [11,12], free layers in spin valves and magnetic tunnel junctions [13,14], flux concentrators or shields [15]. However, amorphous and nanocrystalline thin films very seldom retain the excellent soft magnetic properties of bulk ingots, ribbons and microwires with similar composition [16–18]. In fact, large stresses are often present in as-prepared films as the result of the deposition process [19], and often thermal treatments, even if able to relieve the quenched-in stresses or to induce nanocrystallization, do not succeed to significantly reduce the coercive field [5] because of the static hysteresis component due to the presence of defects and imperfections on the film surface or at the interface with the substrate. In spite of this, moderately soft magnetic properties and high permeability values can be achieved, and suitable thermal treatments with application of magnetic fields can be applied to induce a uniaxial anisotropy in the desired direction.

In order to exploit the soft magnetic properties of amorphous and nanocrystalline films at their best, a comprehensive understanding of their structural and magnetic properties is required. The film thickness strongly influences some important physical and chemical properties, such as composition, atomic order, stresses, magnetic anisotropy, etc. [20,21]. As a function of thickness, significant variations in the coercive field [22] and in the direction of the magnetic anisotropy, through the so-called spin reorientation transition effect [23,34], are observed, which strongly affect the magnetization processes and the magnetic domain configuration of the films. Compared to bulk ingots, ribbons and microwires, amorphous thin films of similar composition are often less stable with temperature, with crystallization processes beginning at lower temperatures [24], and thus require good characterizations to determine the proper thermal treatments and working conditions for specific applications.

* Corresponding author. Tel.: +39 011 3919 855; fax: +39 011 3919 834.
E-mail address: m.coisson@inrim.it (M. Coïsson).

0925-8388/$ – see front matter © 2011 Elsevier B.V. All rights reserved.
doi:10.1016/j.jallcom.2011.01.036

The characterization of thin films poses different challenges with respect to bulk ingots, ribbons or microwires. Many properties of the films being determined by the interaction of the material with the substrate, it is often not possible to detach the film from its substrate to get rid of its contribution from X-ray or thermal analyses. Additionally, the reduced thickness of the samples significantly lowers the signal-to-noise ratio in different kind of characterizations, including XRD, DSC and magnetometry. A sufficiently complete characterization of amorphous and nanocrystalline magnetic thin films thus requires several complementary techniques, which together can be used to acquire a coherent description of their structural and magnetic properties.

Within this framework, in this paper we have prepared $Fe_{84}Nb_{3.5}Zr_{3.5}B_8Cu_1$ (at.%) thin films; this composition is well studied in amorphous and nanocrystalline ribbons because of its high magnetic permeability, low coercivity and high saturation magnetization [25–32]. In our films, the observed dependence of the saturation magnetization on film thickness is interpreted in terms of the development of a α-Fe crystalline phase at the early stages of growth, followed by the formation of the amorphous alloy. The crystallization processes in these films are discussed by means of magnetic measurements at room temperature and as, a function of temperature, on as-prepared and isothermally annealed samples. Transversal Kerr Effect and Mössbauer data support the interpretation given by hysteresis loops and magnetization vs. temperature measurements. Crystallization processes occurring in the films and in ribbons with comparable composition are compared.

2. Experimental

2.1. Experimental techniques

Thin films of a FeZrNbBCu alloy have been prepared by rf sputtering deposition starting from targets made of amorphous ribbons of nominal composition $Fe_{84}Nb_{3.5}Zr_{3.5}B_8Cu_1$ (at.%), prepared with the planar flow casting technique. The substrate was glass. The chamber base pressure was $\approx 2.7 \times 10^{-7}$ mbar, and the Ar plasma pressure was $\approx 1 \times 10^{-2}$ mbar. The rf power was 50 W and typical deposition rates are of the order of 1.07 Å/s. Presputtering time of the target was reduced to 1 min only in order to reduce consumption of the ribbon material, which was only ≈20 μm thick. After calibration of the sputtering rate, several samples with thickness between 5 and 100 nm have been prepared by varying the deposition time. Additionally, a 400 nm thick sample has been sputtered on a resist layer, which has subsequently been dissolved, leaving a number of film flakes detached from the substrate.

Samples elemental composition has been evaluated by means of quantitative microanalysis performed on the sample surface with a Leica Stereoscan 420 scanning electron microscope (SEM) equipped with an Oxford Instruments Link-ISIS system for X-ray energy dispersive spectrometry (EDS). Bulk pure Cobalt was used as a reference material for the calibration of the energy scale. For the quantitative evaluation of the selected elements concentration, measured intensities of X-ray emissions were compared with those of a library of remotely measured standards in the instrument database. A ZAF procedure was applied by the software for the correction of atomic number, absorption and fluorescence errors in the X-rays measured intensity.

X-ray diffraction (XRD) and X-ray reflectivity (XRR) have been performed on the thin films with the Co Kα wavelength in a pseudo-parallel beam configuration. XRD patterns have been collected with an angle of incidence of the X-ray beam on the sample surface fixed at 1°. X-ray diffractograms of the amorphous ribbons used as target and of annealed ribbons have been performed in the Bragg-Brentano configuration. XRR has been used to carefully estimate the samples thickness.

Annealing has been done in furnace in an Ar atmosphere for the ribbons, for times up to 1 h, and in vacuum (a few 10^{-6} mbar) at temperatures up to 650 °C for the films.

Differential scanning calorimetry (DSC) has been performed in order to investigate the thermal behaviour of both ribbons and films. For this purpose, small amounts of sample were inserted in Al crucibles and heated at a constant heating rate of 40 K/min at temperatures up to 600 °C under Ar atmosphere. On each sample, two consecutive heating scans were performed in the same conditions: the first one in order to evaluate the thermal behaviour of the sample, potentially consisting of both reversible and irreversible transformations, the second one aiming at checking the (ir)reversibility of the events observed during the first one and at recording the baseline signal.

Mössbauer spectra were recorded at room temperature, using ^{57}Co:Rh source using a Wissel Mössbauer spectrometer. Conversion electron Mössbauer measurements (CEMS) have been done using a gas flow proportional counter with 95% He + 5% CH_4, in reflection geometry in the case of thin films. Mössbauer spectra of ribbons were measured in transmission geometry, using a conventional proportional counter.

Hysteresis loops have been measured at room temperature (RT) with an alternating gradient field magnetometer (AGFM) with the magnetic field applied in the sample plane. Measurements of magnetization as a function of temperature have been performed with a vibrating sample magnetometer (VSM) equipped with a furnace operating at up to 1000 °C in Ar atmosphere. Also in this case the magnetic field was applied in the sample plane.

Transversal Kerr Effect (TKE) measurements have been performed in the energy range from 0.5 to 4.0 eV, at an angle of incidence of the light equal to 68° and in magnetic fields up to 3.5 kOe. TKE consists in the intensity variation of the p-polarization of light reflected by the sample under magnetization. The value

$$\delta = \frac{I(H) - I(0)}{I(0)} \quad (1)$$

where $I(H)$ and $I(0)$ are the reflected light intensities in the presence and absence of a magnetic field, respectively, was directly measured in the experiment. The alternating magnetic field was aligned parallel to the sample surface and perpendicular to the light incidence plane. The sensitivity of the apparatus was 10^{-5}.

Etching has been performed with the same system used for sputtering, operating at a power of 100 W at reverse polarity. The thickness of samples thinned in this way has been calculated after calibration of etching efficiency (rate ≈0.27 Å/s at an Ar pressure of $\approx 2 \times 10^{-2}$ mbar) and verified by X-ray reflectivity and atomic force microscopy.

2.2. Films composition

The composition of the studied alloy has been determined by means of SEM-EDS microanalysis. Pieces of as-prepared ribbons used as target for sputtering have been analyzed and the results averaged. Since microanalysis is not able to quantify accurately low atomic number elements, such as boron, in Table 1 the nominal composition (first row) has been recalculated as if the alloy would not contain any B (second row). The measured composition on ribbons is reported in the third row, and has to be compared with the one reported in the second row. A rather good agreement with the expected values is obtained, with the amount of copper being below the detection limit (set, by convention, at two times the standard deviation of the background) and thus not reliably estimated.

Table 1
Nominal and measured composition of FeZrNbBCu ribbons and thin films expressed as at.%. Values between parentheses are below two times the standard deviation of the background signal.

	Fe	Cu	Zr	Nb	B
Ribbon (nominal)	84.0	1.0	3.5	3.5	8.0
Ribbon (no B)	91.30	1.09	3.80	3.80	
Ribbon (measured)	91.00	(1.58)	3.81	3.61	
Film (measured)	92.95	(0.45)	2.94	3.66	

For determining the composition of the films, the 400 nm thick sample deposited on a resist and peeled from its substrate has been used, in order to get rid of the signal coming from the glass. Results are reported in the last row of Table 1. The composition of the film closely resembles that of the ribbons, with an increased amount of Fe compensated by slightly less Zr and Nb. As with the ribbons, the Cu amount is too small to be estimated reliably.

The enrichment in Fe of the thin films is worth a few additional comments. When the sputtering process involves an alloy, it is usually assumed that the resulting film will have the same composition as the target, because the elements with higher sputtering yields are removed faster from the target, which then becomes enriched in the elements with a lower yield; under stationary conditions, this process leads to films that preserve the same composition as the target. However, this may not be the case at the beginning of the growth of the films, where mostly the elements with the higher sputtering yields are deposited, thus modifying the sample composition for the first nanometers. Among the elements constituting our alloy, neglecting Cu which is a minor constituent, Fe atoms have the highest sputtering yield: at the ion energy used in the deposition process (≈890 eV), this is 58%, 85% and 112% higher of the ones of B, Nb and Zr atoms, respectively [33]. The higher sputtering rate of Fe atoms with respect to the other species present in the alloy will have an effect on our samples at the early stages of deposition, as will be discussed later.

3. Thickness dependence of magnetization processes

Hysteresis loops of samples with a thickness in the $5 \leq t \leq 100$ nm range have been measured by means of an AGFM. A few examples are reported in Fig. 1. All samples are characterized by a soft magnetic behaviour, with a small coercive field H_C and

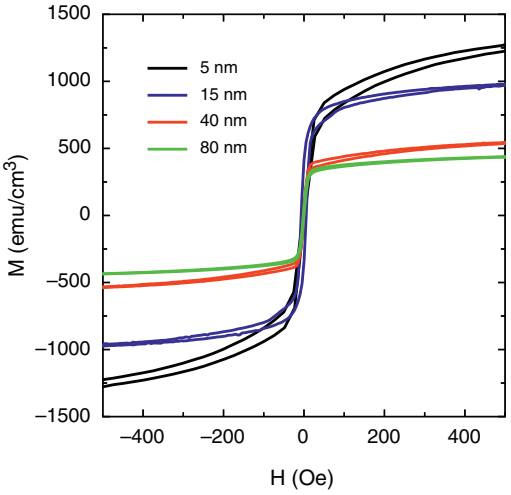

Fig. 1. Hysteresis loops of FeZrNbBCu thin films, at room temperature, in the as-prepared state, for different thickness.

a rather high permeability around H_C. However, thinner samples are characterized by a slower approach to saturation and a higher saturation magnetization M_S; conversely, thicker films are characterized by a much lower M_S value, which is reached more easily.

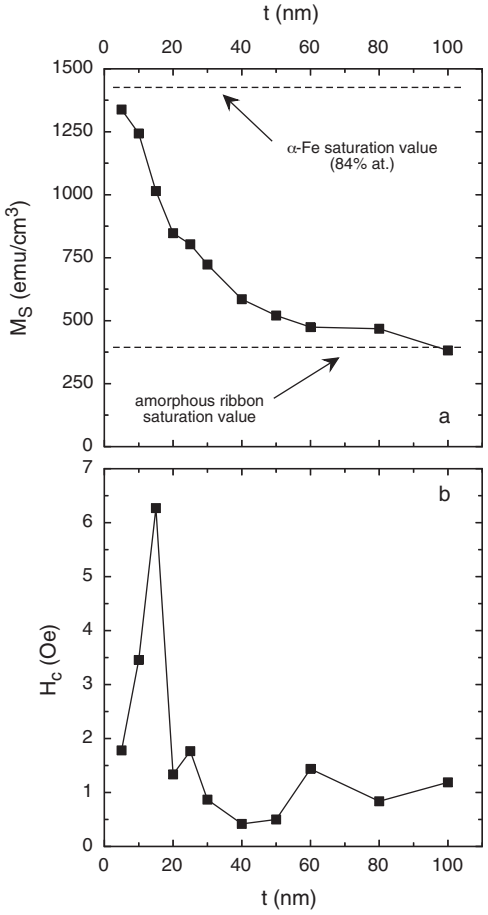

Fig. 2. (a) Saturation magnetization and (b) coercive field as a function of sample thickness in FeZrNbBCu thin films, as-prepared. The dashed lines represent the saturation magnetization of α-Fe at the same concentration as in the studied alloy, and of the as-quenched ribbons.

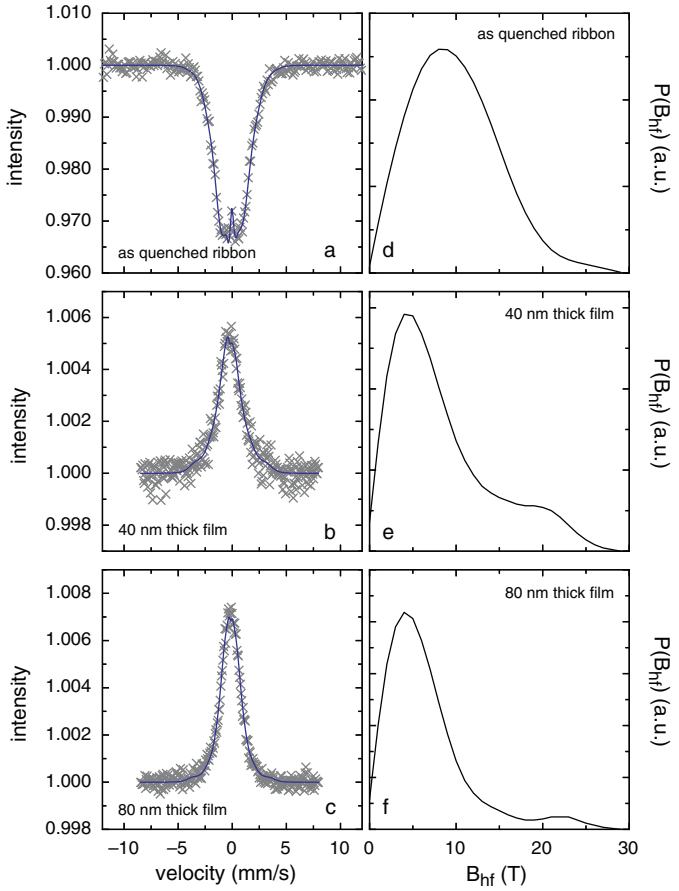

Fig. 3. Left column: Mössbauer spectra of (a) as-quenched ribbon, (b) 40 nm thick film and (c) 80 nm thick film. Symbols: experimental data; full lines: fitted assuming the distribution of hyperfine fields. Right column: Hyperfine field distribution of (d) as-quenched ribbon, (e) 40 nm thick film and (f) 80 nm thick film.

The evolution of the M_S and H_C values as a function of sample thickness is reported in Fig. 2: a monotonic decrease of the saturation magnetization is observed, whereas the coercive field has a maximum slightly above 6 Oe for the 15 nm thick sample, while the other samples have coercivity values all around 1 Oe. It is remarkable that the M_S values cover the full interval ranging from the saturation value of a sample where all the Fe is present in crystalline form (84% α-Fe) and that of the as-quenched ribbons [5].

Apparently, a microstructural evolution of the samples, in the as-prepared state, as a function of thickness is observed, with thinner films closer to a fully crystalline state and thicker films closer to a fully amorphous state. To further investigate this subject, we proceeded to measure X-ray diffraction patterns of selected films. Unfortunately, it was impossible to detect the crystalline fraction of the thinner films by means of XRD measurements, even with the low-incidence-angle pseudo-parallel beam technique: as a matter of fact, the XRD patterns of 5, 10 and 15 nm films were essentially identical to the one of the bare substrate, owing to the very small amount of material responsible for X-ray scattering. A broad halo due to the metallic amorphous matrix became detectable in the XRD patterns of all studied films starting from a thickness of 25 nm. No evidence of crystalline peaks appeared in any of the patterns of thicker films.

To overcome the intrinsic limits of XRD technique regarding thin films, we performed a set of Mössbauer investigations on as-quenched ribbons and selected films of different thickness. Results are reported in Fig. 3, where on the left column the intensity of the measured signal is reported as a function of sample velocity, and

on the right column the hyperfine field B_{hf} distribution is plotted. Fig. 3(a) reports the spectrum of the as-quenched ribbon: it can be clearly seen that the sextet typical of ferromagnetic materials has almost disappeared, which could be due to the fact that the Curie temperature of the amorphous alloy is rather close to room temperature; this will be discussed in Section 4. The same discussion applies to the spectra of the two films. The hyperfine field distribution obtained from the fitting of the spectra shows, in the case of the as-quenched ribbon (Fig. 3(d)), that the distribution is peaked at rather low B_{hf} values (B_{hf} of pure Fe should be 33.33 T); this suggests that most Fe atoms have non magnetic atoms (e.g. B, Nb, Zr) in their first-neighbour shell, which further confirms the amorphous state of the as-quenched ribbon. A similar discussion can be made concerning the 80 nm thick sample, whose B_{hf} distribution is shown in Fig. 3(f). Its comparison with the B_{hf} distribution of the film having a thickness of 40 nm suggests that both samples are characterized by a predominant amorphous phase, but the thinner film (Fig. 3(e)) displays a hyperfine field distribution with a more pronounced shoulder at high B_{hf} vaues, suggesting the presence, together with the amorphous phase, of a minority crystalline phase where Fe atoms are most likely surrounded by other atoms of the same kind. This could account for the increase of saturation magnetization on reducing the film thickness, as discussed in Fig. 2.

Our interpretation, following the considerations presented in Section 2.2, is that for the first nanometers Ar ions in the plasma sputter mostly Fe atoms, due to their higher sputtering yield. Only after a time corresponding, for our rate, to the deposition of a ≈20 nm film (several minutes), the flow of particles ejected from the target reaches a stationary condition, and the sputtered material has the same composition as the alloy of the target. In this way, the film first grows mostly crystalline (α-Fe, saturation magnetization close to that of Fe as shown in Fig. 2), owing to the lack of glass-forming elements, then an increasing amount of Zr, Nb, B and Cu are sputtered until the amorphous alloy grows on top of the first thin, crystalline layer. As thickness is increased, the role of the deepest Fe layer in determining the saturation value becomes less important, and M_S progressively reduces toward the value found on amorphous ribbons. When the thickness is above ≈100 nm the role of the α-Fe layer is negligible, and the film appears as fully amorphous. Also the composition of sufficiently thick films becomes close to that of the ribbons, although possibly slightly enriched in Fe (because of the crystalline deep layer), as confirmed by the microanalysis reported in Table 1.

4. Annealing and crystallization process

By assuming that the films start growing crystalline and progressively develop an amorphous phase with a composition close to that of the ribbons used as targets, one can expect very different properties as a function of temperature and very different crystallization processes, because of their different microstructure in the as-prepared state.

In order to investigate the crystallization process of the studied alloy, we first performed a differential scanning calorimetry on an as-quenched ribbon and on some flakes of the 400 nm thick film, which, due to its thickness, is mostly composed of the amorphous phase. The DSC scans, obtained in a heating rate of 40 K/min, after subtraction of the baseline signal, are shown in Fig. 4. The as-quenched ribbon displays a strong crystallization peak, with a crystallization onset temperature $T_x \approx 504\,^\circ$C due to the α-Fe precipitation. Conversely, the thin film displays a similar peak, although at lower temperatures ($T_x \approx 440\,^\circ$C), preceded by a large shoulder extending over the range 360–460 °C. Such kind of broad exothermic signal preceding crystallization events has been observed on several amorphous thin films of different composition [5,34,35] and may be related to an irreversible process such as the growth of pre-existing crystals and, possibly, surface oxidation, which plays a major role in free-standing thin films due to their very high surface/volume ratio (more than 50 times larger compared to the one of the ribbon form). A smaller peak, centered at ≈294 °C, marks a first crystallization process. Although at a rather low temperature, above 300 °C irreversible effects are detected in the microstructure and magnetic properties of the samples, as will be discussed in the following. We believe that this first crystallization peak has to be attributed to the development of a small volume of α-Fe phase in the amorphous matrix, possibly in deep layers of the sample where the composition is particularly rich in Fe, as will be discussed later. Undoubtedly, a TEM characterization would certainly provide helpful data to clarify the exact nature of the crystalline phase that develops in the thin films at such low temperatures. In absence of such an analysis, several complementary techniques have been used to study the crystallization processes in our samples, and their effects of the magnetic properties.

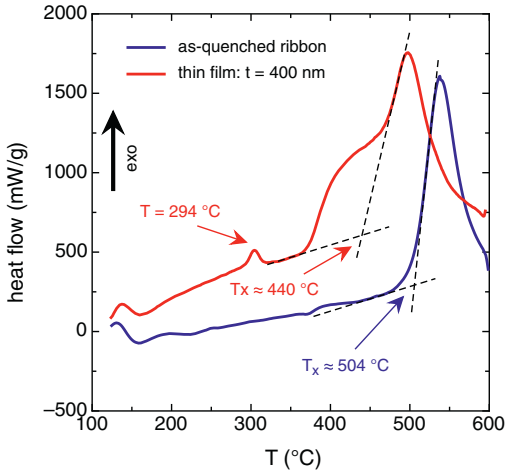

Fig. 4. DSC curves (heat flow vs. temperature) at 40 K/min of as-quenched ribbon (blue curve) and flakes of the 400 nm thick film (red curve). (For interpretation of the references to color in this figure legend, the reader is referred to the web version of the article.)

An overview of the effects of annealing on the magnetic properties of the studied alloy is reported in Fig. 5, for both ribbons and thin films, where the magnetization, measured as a function of temperature, is reported for both ribbons and thin films. In the case of ribbons (panel (a)), the as-quenched sample is shown, together with selected specimens annealed at 470, 490 and 510 °C in Ar atmosphere for 60 min. In the case of the as-quenched sample, the magnetization rapidly drops to zero at about 100 °C, marking the Curie temperature of the amorphous alloy. Only at about 450 °C irreversible processes appear, in the form of the precipitation of a crystalline phase with a higher Curie temperature, resulting in an increase of the magnetization. This temperature value is in good agreement with the one determined by DSC (see Fig. 4); in the case of M vs. T measurements, the lower heating rate (≈2 K/min) accounts for the slightly lower temperature at which crystallization is seen to begin. The precipitated crystalline phase is most probably α-Fe, as demonstrated by the temperature at which magnetization drops again to zero (≈760 °C), compatible with the Curie temperature of iron.

For the ribbon that has previously been annealed at 470 °C similar arguments apply, with the important difference that the sample, even before heating it up to 800 °C, already has a crystalline phase; this is evidenced by the fact that, upon reaching the Curie temperature of the amorphous phase, the magnetization is not zero.

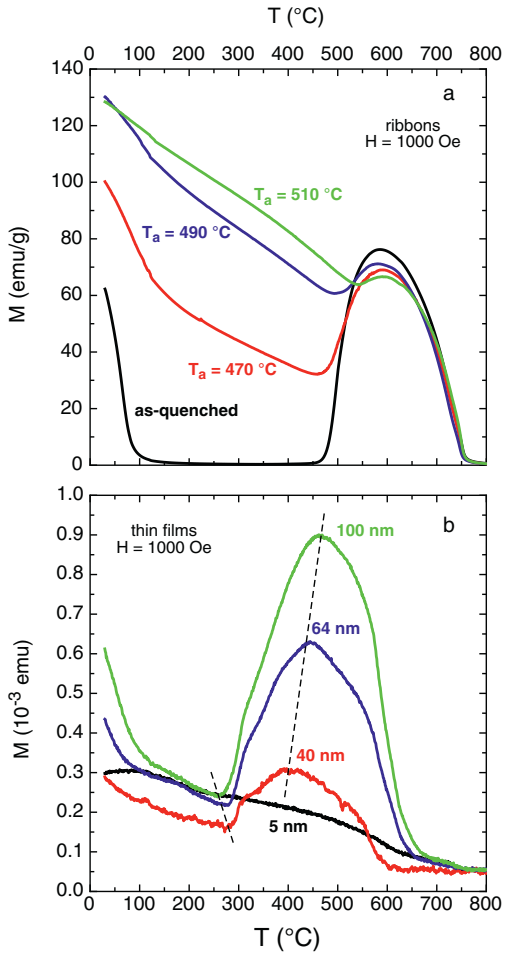

Fig. 5. (a) *M* vs. *T* performed on ribbons, up to 800 °C, under a field of 1000 Oe, on as-quenched and annealed samples (470, 490 and 510 °C in Ar atmosphere for 60 min). (b) *M* vs. *T* performed on thin films, up to 800 °C, under a field of 1000 Oe, on as-prepared samples with different thickness.

The transition from ferromagnetic to paramagnetic of the amorphous phase is marked by a change of slope of the *M* vs. *T* curve, which would apparently reduce to zero again at ≈760 °C. However, further crystallization occurs at slightly below 500 °C, following a path close to the one observed on the as-quenced sample. A similar behaviour is observed on the other annealed samples, which, due to the higher temperatures at which have been annealed, display progressively reduced amorphous phases (almost undetectable on the sample annealed at 510 °C) and crystallization peaks.

For all ribbons, when the temperature is decreased, after reaching 800 °C the magnetization increases monotonically down to room temperature (not shown in the figure, for clarity), thus putting into evidence the occurrence of irreversible effects (crystallization) during the heating process.

In the case of thin films (Fig. 5(b)), the 100 nm thick sample closely resembles the as-quenched ribbon, with the same Curie temperature of the amorphous phase, but with two notable exceptions: upon reaching the Curie temperature of the amorphous phase, the magnetization does not reduce to zero, indicating that a crystalline component is already present in the sample (as suggested previously), and the crystallization peak begins at ≈270 °C, in good agreement with the small crystallization peak observed on the thin film by DSC (Fig. 4). After the crystallization peak, the magnetization drops to zero at a lower temperature with respect to the ribbon: this could be due to the fact that borides have already started to form, reducing the contribution of the α-Fe phase (which has a higher Curie temperature), but we could not exclude severe damage to the samples, since the glass substrate melts above ≈650 °C, and a measurement of the films magnetization above this temperature could be not reliable.

An effect of thickness on the crystallization process in thin films is clearly seen in Fig. 5(b): while the 64 nm thick sample behaves similarly to the 100 nm one, the 40 nm thick specimen is characterized by a much less significant amorphous phase (it is much more difficult to detect its Curie temperature), and correspondingly the crystallization peak is less pronounced. On further reducing thickness, as shown for example on the 5 nm thick sample, no crystallization peak is observed, suggesting that the sample is fully crystalline. Both the beginning of the crystallization process and the *M* vs. *T* peak show a marked dependence on the film thickness, as evidenced by the dashed lines in Fig. 5(b).

The crystallization temperatures are remarkably different between ribbons and thin films, indicating that the starting microstructural configuration is completely different. Even though both DSC and *M* vs. *T* measurements point to the occurrence of irreversible structural processes on thin films at temperatures as low as ≈300 °C, this rather low temperature claimed for further investigations. To this aim, three samples (a film having a thickness of 100 nm, a flake with a thickness of 400 nm detached from its substrate and an as-quenched ribbon) have been submitted to three subsequent annealings, at 250, 350 and 440 °C, respectively. These thermal treatments were performed in the DSC chamber in order to reproduce the same conditions as during the DSC measurements (atmosphere and heating rate). Before and after each DSC annealing, hysteresis loops have been measured by means of an AGFM. The results are compared in Fig. 6. In the case of the ribbon, all three annealing temperatures are well below the crystallization peak (see Fig. 4), and in fact the hysteresis loops are largely superimposed, with just a small stress relaxation responsible for a slightly increased low field permeability of the sample. Conversely, the two films, independently on thickness and on the presence or absence of the substrate, show a very different behaviour: upon heating up to 250 °C, no significant variation is observed in the hysteresis loop. When temperature is increased at 350 °C, the saturation mag-

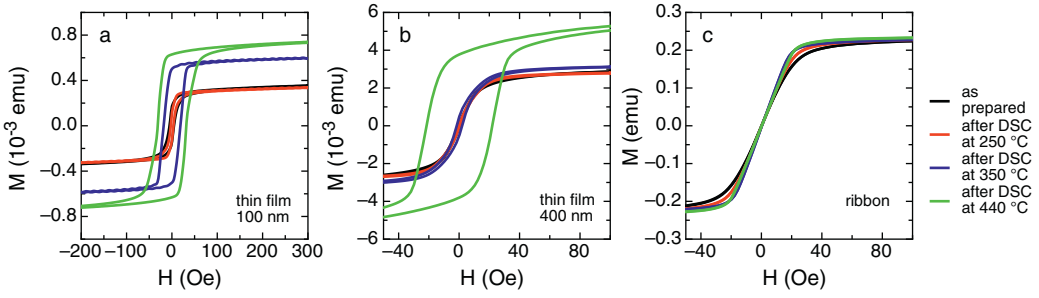

Fig. 6. Hysteresis loops on samples as-prepared and heated up to 250, 350 and 440 °C by means of a DSC equipment, on (a) thin film of 100 nm, (b) thin film of 400 nm detached from its substrate, (c) as-quenched amorphous ribbon.

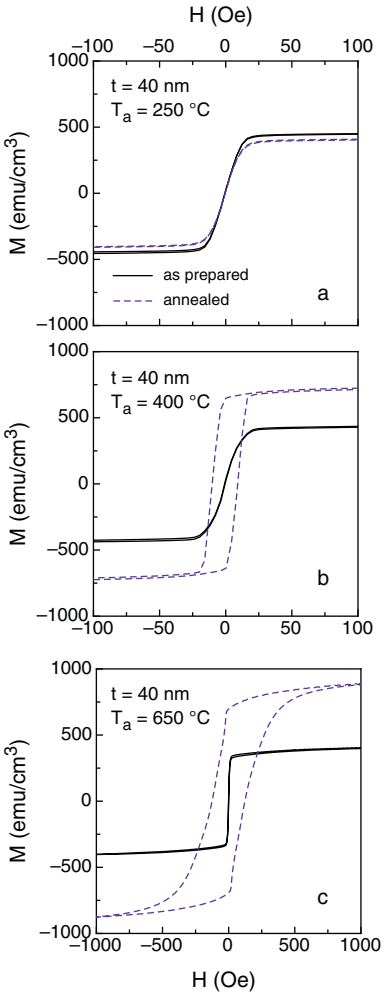

Fig. 7. Hysteresis loops performed on thin films having a thickness of 40 nm, before (black continuous line) and after (blue, dashed line) annealing at (a) 250 °C, (b) 400 °C, (c) 650 °C. (For interpretation of the references to color in this figure legend, the reader is referred to the web version of the article.)

netization increases, indicating the precipitation of α-Fe, and the coercive field increases, although the latter effect is less evident in the 400 nm thick film probably because the absence of the substrate allows more effective stress relaxations, that soften the magnetic properties of the specimen. When DSC is performed at 440 °C, saturation magnetization increases even more, and a much harder magnetic behaviour is observed, indicating a significant precipitation of a crystalline phase, in spite of the relatively low temperature, which does not affect by any means the magnetic properties of the ribbons.

As a consequence of these results, thin films of all available thickness have been submitted to isothermal annealing in furnace in vacuum for 60 min at temperatures in the interval $200 \leq T_a \leq 650$ ° C. Hysteresis loops have been measured on each sample before and after annealing. Selected results are shown, as an example, in Fig. 7 for the thin films with a thickness of 40 nm at three annealing temperatures (Note that in Fig. 7(c) the horizontal scale is different). Upon annealing below 300 °C, no significant variation of the hysteresis loop is observed, confirming what already discussed previously. Conversely, at temperatures above 300 °C a progressive increase of saturation and coercivity is observed. However, this effect is thickness dependent.

The evolution of the coercive field as a function of annealing temperature for a few films with different thickness is shown in Fig. 8. For $T_a \leq 300$ ° C a slight reduction of the coercive field is

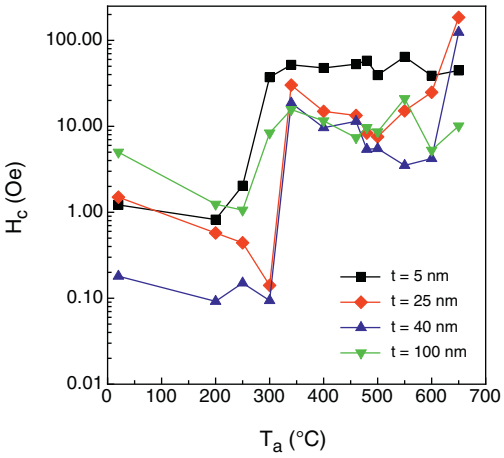

Fig. 8. Annealing temperature dependence of coercive field in thin films with different thickness.

observed on all samples, probably due to stress relaxation effects. Above 300 °C, the coercive field abruptly increases, marking an irreversible change in the microstructure of the material. However, the saturation magnetization does not follow the same path, as shown in Fig. 9, which, as a function of film thickness, plots the relative variation of the saturation magnetization of the annealed samples, before and after the annealing process. Samples with a thickness lower than ≈20 nm, whose M_S is rather large (see Fig. 2) and thus are in a predominantly crystalline state, after annealing above 300 °C display a significant reduction of the saturation magnetization, probably due to the precipitation of harder crystalline phases (such as borides). Conversely, thicker samples, which display a progressively more dominant amorphous phase, do not significantly change their M_S for annealing temperatures ≤300 °C, but increase their magnetization by a factor up to 2 when thickness is sufficiently high and most of the sample, before annealing, is amorphous (64 and 100 nm thick samples).

These results are confirmed by TKE measurements; selected results are reported in Fig. 10. For both samples annealed at 200 °C, the TKE signal remains almost constant with increasing energy; this indicates that the samples are mainly in an amorphous state [36,37], at least for 15–25 nm below the samples surface (in fact, this is the penetration depth of the light used for making these measurements). This is in agreement with Fig. 2, where samples

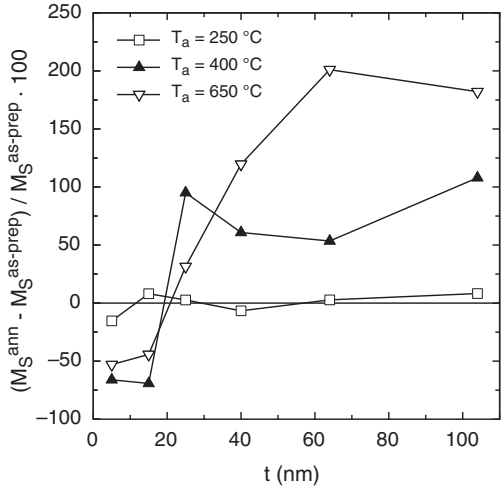

Fig. 9. Relative variation of the saturation magnetization as a function of film thickness for selected annealing temperatures.

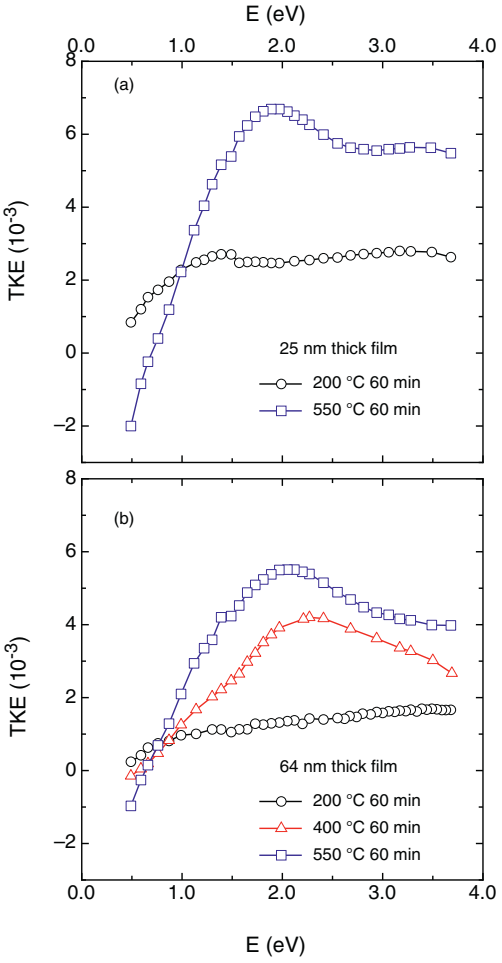

Fig. 10. (a) Spectral dependences of TKE for 25 nm thick films, annealed at 200 and 550 °C. (b) TKE spectra for 64 nm thick films, annealed at 200, 400 and 550 °C.

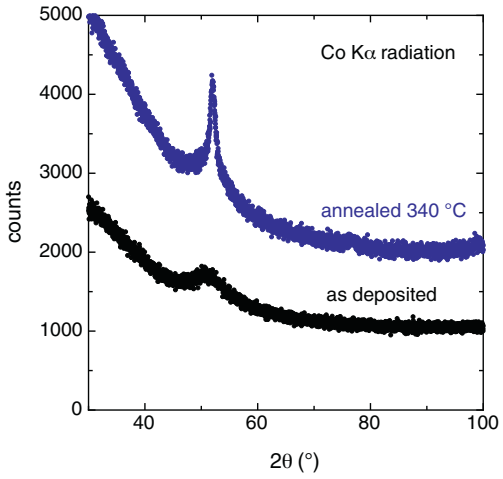

Fig. 11. X-ray diffraction patterns of the 80 nm thin film in the as deposited state and after a 60 min annealing at 340 °C.

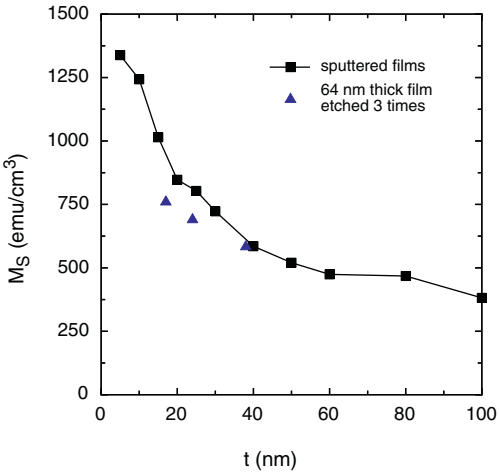

Fig. 12. Saturation magnetization values as a function of film thickness. Black squares: sputtered films with different thickness. Blue triangles: 64 nm thick film, submitted to three consecutive etching processes. (For interpretation of the references to color in this figure legend, the reader is referred to the web version of the article.)

with a thickness of 25 nm already displayed a significant drop of saturation magnetization toward the value of the amorphous alloy, and with Fig. 8, which shows that annealing at 200 °C does not significantly affect structural and magnetic properties, for any film thickness. Conversely, if the annealing temperature is increased, TKE measurements reported in Fig. 10 are characterized by a much stronger dependence on energy, indicating the occurrence of a significant crystallization of the samples. Again, this is in agreement with the previously discussed results.

The phase composition of selected isothermally annealed thin films has been studied by means of XRD. In Fig. 11 the diffraction patterns of the 80 nm thin film in the as prepared state and after a 60 min annealing at 340 °C are reported: while the as deposited film appears fully amorphous at XRD, for the reasons stated above, the development of a crystalline fraction of α-Fe in coexistence with the amorphous matrix can be detected after heat treatment at 340 °C, despite the low signal-to-noise ratio due to the scarcity of scattering material. The decreasing shape of the background signal at low angles is due to the amorphous halo contribution of the glass substrate.

5. Etching

The previous discussion assumes, as suggested by the many evidences in the measurements reported so far, that the first few nanometers of the thin films are made of α-Fe, while subsequent growing of the sample results in an amorphous alloy close to the composition of the ribbons used as targets. To give an additional proof of this interpretation, we chose a 64 nm thick sample and proceeded to thin it with subsequent plasma etching sessions. After each of those, the resulting film thickness has been determined by means of XRR, and hysteresis loops have been measured; the saturation magnetization has been recorded, and is reported in Fig. 12, together with the M_S data already reported in Fig. 2. The figure clearly indicates that upon progressively reducing the film thickness by means of sputter etching, the saturation magnetization increases, with a trend that closely resembles the M_S vs. t behaviour of the films sputtered with different thickness. The subsequent etching processes, then, progressively remove the amorphous material, whose contribution to the total magnetization becomes increasingly less important with respect to that of the crystalline phase present in the deepest layers.

6. Conclusions

FeZrNbBCu thin films have been prepared with different thickness, and their magnetic properties have been studied. A decrease of the saturation magnetization with increasing film thickness has been interpreted in terms of the presence of a crystalline α-Fe

phase at the early stages of film growth, followed by the deposition of the amorphous alloy. This interpretation has been validated by submitting the studied films to thermal treatments, either with continuous monitoring of the magnetization, or isothermal annealing with subsequent measurement of hysteresis loops at room temperature. Thinner films, which have a significant crystalline phase in the as-prepared state, display less prominent crystallization features, whereas thicker films, with a significant amorphous phase in the as-prepared state, are characterized by much more pronounced crystallization effects. Additionally, progressive thinning of a film by means of sputter etching allows to reduce the amorphous component, leading to the expected increase of saturation magnetization as the thickness decreases. Mössbauer and Transversal Kerr Effect measurements confirm this view.

Finally, the crystallization process of the thin films has been compared with that of amorphous ribbons having similar composition; in thin films, the crystallization processes of the amorphous phase begin at much lower temperatures with respect to the ribbons and always lead to a magnetic hardening of the material, in contrast to what is the usual behaviour of the nanocrystalline FeZrNbBCu melt-spun alloy.

Acknowledgment

This work has been partly performed at NanoFacility Piemonte, INRiM, a laboratory supported by Compagnia di San Paolo.

References

[1] G. Herzer, Encyclopedia of Materials: Science and Technology, Elsevier, 2001, pp. 149–156.
[2] F. Mazaleyrat, R. Barrué, Handbook of Advanced Electronic and Photonic Materials and Devices, 2001, pp. 59–102.
[3] G. Herzer, J. Magn. Magn. Mater. 157–158 (1996) 133–136.
[4] K. Hashimoto, in: S. Steeb, H. Warlimont (Eds.), Rapidly Quenched Metals, vol. II, North-Holland(Amsterdam), 1985, pp. 1449–1456.
[5] F. Celegato, M. Coïsson, E. Olivetti, P. Tiberto, F. Vinai, Phys. Stat. Sol. A 205 (2008) 1745–1748.
[6] K. Suzuki, A. Makino, A. Inoue, T. Masumoto, J. Appl. Phys. 70 (1991) 6232.
[7] B. Ahamada, F. Alves, R. Barrué, J. Magn. Magn. Mater. 242–245 (2002) 1443–1445.
[8] G. Vértesy, B. Idzikowski, J. Magn. Magn. Mater. 299 (2006) 112–119.
[9] R. Hasegawa, D. Azuma, J. Magn. Magn. Mater. 320 (2008) 2451–2456.
[10] J. Petzold, J. Magn. Magn. Mater. 242–245 (2002) 84–89.
[11] K. Tanahashi, A. Kikukawa, Y. Takahashi, Y. Hosoe, Appl. Phys. 93 (2003) 6766.
[12] J. Yu, C.H. Chang, D. Karns, G.P. Ju, Y. Kubota, W. Eppler, C. Brucker, D. Weller, J. Appl. Phys. 91 (2002) 8357–8359.
[13] S. Ikeda, J. Hayakawa, Y. Ashizawa, Y.M. Lee, K. Miura, H. Hasegawa, M. Tsunoda, F. Matsukura, H. Ohno, Appl. Phys. Lett. 93 (2008) 082508.
[14] J.U. Cho, D.K. Kim, R.P. Tan, S. Isogami, M. Tsunoda, M. Takahashi, Y.K. Kim, IEEE Trans. Magn. 45 (2009) 2364–2366.
[15] P. Ripka, Magnetic Sensors and Magnetometers, Artech House Publishers, Boston, 2001.
[16] C. Chang, B. Shen, A. Inoue, Appl. Phys. Lett. 89 (2006) 051912.
[17] F. Li, B. Shen, A. Makino, A. Inoue, Appl. Phys. Lett. 91 (2007) 234101.
[18] M. Vázquez, A.P. Zhukov, J. Magn. Magn. Mater. 160 (1996) 223–228.
[19] H. Windishmann, Crit. Rev. Sol. St. Mater. Sci. 17 (1992) 547–596.
[20] P. Sharma, H. Kimura, A. Inoue, E. Arenholz, J.H. Guo, Phys. Rev. B 73 (2006) 052401.
[21] A.D.C. Viegas, M.A. Correa, L. Santi, R.B. da Silva, F. Bohn, M. Carara, R.L. Sommer, J. Appl. Phys. 101 (2007) 033908.
[22] T.A. Moore, J. Rothman, Y.B. Xu, J.A.C. Bland, J. Appl. Phys. 89 (2001) 7018.
[23] M. Carubelli, O.V. Billoni, S.A. Pighin, S.A. Cannas, D.A. Stariolo, F.A. Tamarit, Phys. Rev. B 77 (2008) 134417.
[24] G. Peto, I. Szabo, E. Kisdi-Koszo, L. Guczi, P. Kollar, J. Magn. Magn. Mater. 140 (1995) 425.
[25] M.E. McHenry, F. Johnson, H. Okumura, T. Ohkubo, V.R.V. Ramanan, D.E. Laughlin, Scr. Mater. 48 (2003) 881–887.
[26] A. Makino, T. Hatanai, Y. Naitoh, T. Bitoh, A. Inoue, T. Masumoto, IEEE Trans. Magn. 33 (1997) 3793.
[27] S.S. Modak, N. Ghodke, F. Mazaleyrat, M. LoBue, L.K. Varga, A. Gupta, S.N. Kane, J. Magn. Magn. Mater. 320 (2008) e828–e832.
[28] K. Zhang, B. Han, L. Xiao, Z. Hua, D. Zhou, T. Zhang, X. Du, B. Yao, X. Xun, D. Wang, J. Phys. D: Appl. Phys. 40 (2007) 6507–6513.
[29] F. Celegato, M. Coïsson, S.N. Kane, F. Mazaleyrat, S.S. Modak, P. Tiberto, L.K. Varga, F. Vinai, Phys. Stat. Sol. A 205 (2008) 1749–1752.
[30] A. Michels, C. Vecchini, O. Moze, K. Suziki, P.K. Pranzas, J. Kohlbrecher, J. Weissmüller, Phys. Rev. B 74 (2006) 134407.
[31] W. Quin, Y.F. Zhang, Y.W. Du, F. Xu, Y.J. Wu, M. Zhao, F. Ma, J. Magn. Magn. Mater. 270 (2004) 174–181.
[32] A. Hsiao, M.E. McHenry, D.E. Laughlin, M.J. Kramer, C. Ashe, T. Ohkubo, IEEE Trans. Magn. 38 (2002) 3039.
[33] N. Laegreid, G.K. Wehner, J. Appl. Phys. 32 (1961) 365–369.
[34] M. Coïsson, F. Celegato, E. Olivetti, P. Tiberto, F. Vinai, M. Baricco, J. Appl. Phys. 104 (2008) 033902.
[35] F. Celegato, M. Coïsson, P. Tiberto, F. Vinai, M. Baricco, Phys. Stat. Sol., doi:10.1002/pssc201000197, in press.
[36] L. Valenchik, E.A. Gan'shina, V.S. Guschin, D.N. Djuraev, G.S. Krinchik, Fiz. Met. Metalloved 67 (1989) 1108.
[37] E.A. Gan'shina, N.S. Perov, M.Yu. Kochneva, P.M. Sheverdyaeva, C.G. Kim, C.O. Kim, J. Magn. Magn. Mater. 239 (2002) 484–486.